The development of thermodynamically-consistent and physics-informed equation-of-state model through machine learning

J. Hinz[1,*], Dayou Yu[2], Deep Shankar Pandey[2], Hitesh Sapkota[2], Qi Yu[2], D. I. Mihaylov[1], V. V. Karasiev[1,,†], and S. X. Hu[1,3,4]

[1]Laboratory for Laser Energetics, University of Rochester, Rochester NY, 14623
[2] Rochester Institute of Technology, Rochester NY, 14623
[3]Department of Physics and Astronomy, University of Rochester, Rochester NY, 14627
[4]Department of Mechanical Engineering, University of Rochester, Rochester NY, 14611
[*] jhin@lle.rochester.edu
[†] vkarasev@lle.rochester.edu

Ab initio molecular dynamic (AIMD) simulations have become an important tool used in the construction of equations of state (EOS) tables for warm dense matter. Due to the computational costs only a limited number of system states conditions can be simulated, and the remaining EOS surface must be interpolated for use in radiation-hydrodynamic simulations of experiments. In this work we develop a thermodynamically consistent EOS model that utilizes a physics informed machine learning approach to implicitly learn the underlying Helmholtz free-energy from AIMD generate energies and pressures. The model, referred to as PIML-EOS, was trained and tested on warm dense polystyrene producing a fit within a 1% relative error for both energy and pressure and is shown to satisfy both the Maxwell and Gibbs-Duhem relations. In addition, we provide a path towards obtaining thermodynamic quantities such as the total entropy and chemical potential (containing both ionic and electronic contributions) which are not available from current AIMD simulations.

Section I: Introduction

The development of reliable equations of state (EOS) is fundamental to furthering the understanding of material properties. This is particularly true for warm dense matter (WMD) systems which have both a solid-state density and a thermal energy comparable to the Fermi energy. In this regime, accurate and fully consistent EOS are required for the closure of the fluid equations governing hydrodynamic simulations which are utilized to investigate spherical target implosions in inertial confinement fusion (ICF) research [1-8] and in some cases used to determine the full thermodynamic state of experimentally measured systems [9,10]. Beyond ICF research, EOS also play a key role in planetary science: reliable EOS tables are utilized in studies of planetary evolution and collisions [11], as well as to provide insights into intraplanetary dynamics [12-14].

A standard approach to constructing EOS is often a semi-empirical one where a first principles-based EOS with adjustable free parameters is fit to experimental measurements [15-21]. However, in the WDM regime experimentally producing target temperatures and densities is a challenging task. In most cases the sampling of the EOS surface is often limited to a few points primarily confined to the principle Hugoniot [9,10,22-25] leaving portions of a material's EOS

experimentally unexplored. Furthermore, the underlying form of a first principles-based EOS may have limited ability to accurately describe the WDM system. Such is the case in QEOS [26] and SESAME [19] where the Thomas-Fermi model [27], known for its inability to bind molecules, is often used to describe the electronic contribution to the constructed EOS. When these two EOS are compared to results based on state-of-the-art density functional theory (DFT) treatment of the electrons, significant differences can be observed in the predicted Hugoniot and in the resulting simulated implosions [4-8]

An alternative approach to constructing EOS tables is to utilize *ab initio* molecular dynamics (AIMD) simulations [4-8,28,29]. Although this approach has been made possible by the increase in computing power over the past few decades, on-the-fly calculations of a material's EOS in the WDM regime are still prohibitively costly. Therefore, an EOS is often calculated at a few hundred temperature and density conditions, at most [28], to produce a grid of EOS values across the domain of temperature and density of interest. The intermediate values of the EOS surface are then obtained by applying an interpolation scheme to the calculated points. A key factor in the reliability of this approach is ensuring the interpolation scheme provides thermodynamically consistent energies and pressures, which is often overlooked.

One of the earliest interpolation schemes with built in thermodynamic consistency was the bi-quintic scheme put forth by Swesty [30] in which the Helmholtz free-energy of a system was directly interpolated. The challenge of utilizing such an interpolation scheme for EOS data generated by AIMD simulations is the total Helmholtz free-energies are unavailable (this is also the case for the total entropies and chemical potentials). This issue was later circumvented by Dilts [31] where thermodynamic constraints were directly enforced in a tuned regression estimator method that utilized a set of monomials to simultaneously interpolate the available energy and pressure data. In recent years, the underpinnings of Swesty and Dilts works have lived on in the context of machine learning (ML) based schemes where neural networks [32-38] or Gaussian process regressions [39,40] have been trained to learn EOSs. In the work of Gaffney *et al* [39], the use of AIMD training data in the direct modeling of the Helmholtz free-energy produced excellent interpolations for the energy and pressure of warm dense B_4C. However, not all thermodynamic relations were confirmed to hold (e.g. Gibbs Duhem relation), nor was it clear if any information is missing from the implicitly learned Helmholtz free-energies. Additionally, many of the other current ML based EOS models have been primarily applied to cases where synthetic data can be easily obtained and where most, if not all, EOS quantities are available. Such models may not be suitable for use with AIMD training data due to the missing thermodynamic quantities.

In the present work, we aim to address the above concern by constructing a physics informed ML based EOS, referred to as PIML-EOS, that utilizes only available energy, pressure, temperature and density data from AIMD simulations. A thorough check of the level of thermodynamic consistency of the model will be provided. Additionally, we will demonstrate a potential path towards obtaining thermodynamic quantities that are currently unavailable from the direct output of AIMD simulations. The rest of the paper is outlined as follows. Section II provides details about the reference data set and data scaling. Section III defines the criteria for

thermodynamic consistency. Section IV provides details on the construction of the model. And section V contains the results and discussion before the work is concluded in section VI.

Section II: Reference data

Data set: Having a reliable EOS for warm dense polystyrene (CH) is of importance due to its utilization as an ablator material in ICF implosions [7,29]. As polystyrene has been extensively studied, EOS data is readily available. Here, the data from Zhang *et al* [29] for polystyrene with equal parts carbon and hydrogen will be used as a test of the proof of principle of the PIML-EOS model constructed in Section IV. Shown in Fig. 1a are the temperature and density points comprising the reference data set. For simplicity, the original set of conditions has been truncated to form a rectangular domain of reference data where the densities vary between 2.1 and 12.6 g/cm^3. The temperature range was not affected by this truncation and the full range from 6.7x10^3 to 1.3x10^8 K is considered. The corresponding target internal energies range from -10^3 to 1.5x10^5 eV/CH and the pressures range from 44 to 9.4x10^6 GPa. At temperatures below 10^6 K, the reference data was obtained with AIMD simulations driven by Kohn-Sham DFT. Above 10^6 K path integral Monte Carlo (PIMC) based AIMD simulations were utilized. The DFT based energies were then shifted to match within 21.8 eV/CH at 10^6 K (this will be referred to as the matching boundary). For additional details about the calculation of the reference data see [29].

Scaling relations: Before constructing the PIML-EOS model all thermodynamic quantities are made dimensionless. To achieve this, a value of E_0 and ρ_0 must be set to scale the energy and density respectively. These values can be chosen independently but should be representative of the values found in the reference data set. For the polystyrene data set described above, E_0 and ρ_0 were chosen to be 100 eV and 2.1 g/cm^3 respectively. Additionally, with the use of Boltzmann's constant, k_B, and the mass of a CH pair, m, all remaining thermodynamic quantities can be made dimensionless. Furthermore, all extrinsic variables are transformed to intrinsic variable with a scaling by N_0, the number of CH pairs in the system. Due to the 1:1 ratio of C to H, this choice enables the system to be treated as a single component system. For further details on the scaling relations see table I. Moving forward, all thermodynamic quantities and equations should be assumed to be dimensionless and describe intrinsic quantities unless stated otherwise.

Table I: Definition and scaling relation for all thermodynamic quantities.

Quantity	Symbol	Scaling
Density	ρ	$\frac{1}{\rho_0}$
Temperature	T	$\frac{k_B}{E_0}$
Energy (internal)	E	$\frac{1}{N_0 E_0}$

Helmholtz free energy	F	$\frac{1}{N_0 E_o}$
Entropy	S	$\frac{1}{N_0 k_B}$
Pressure	P	$\frac{m}{\rho_0 E_0}$
Chemical potential	μ	$\frac{1}{E_0}$

Section III: Thermodynamic consistency

For an interpolation scheme to be thermodynamically consistent the predicted energies and pressures must be in accordance with the definitions for the associated thermodynamic potential [30,31,41]. Additionally, both Maxwell's relation [30,31,35,39,41] and the Gibbs-Duhem relation [41] must be satisfied. The latter of which has not been thoroughly explored in the context of ML interpolation schemes. The predicted pressures and entropies of the interpolation scheme should also be non-negative and in the context of a single phase the corresponding stability conditions for the thermodynamic potential must be met [30,31,35,41].

Definitions: Given that the polystyrene reference data set contains temperatures, T, and densities, ρ (two independent variables), the natural thermodynamic potential to work in is that of the Helmholtz free-energy, $F(T,\rho)$. From the Helmholtz free-energy, the energy, E, and pressure, P, are defined as

$$E = F + TS = F - T\frac{\partial F}{\partial T}, \tag{1}$$

and

$$P = \rho^2 \frac{\partial F}{\partial \rho} \tag{2}$$

where S is the entropy.

Maxwell's relation: In terms of the Helmholtz free-energy, Maxwell's relation is a statement about the commutativity of the partial derivatives of temperature and density [30,41],

$$\frac{\partial^2 F}{\partial T \partial \rho} = \frac{\partial^2 F}{\partial \rho \partial T}. \tag{3}$$

Using Eqs. (1) and (2), the Maxwell's relation of Eq. (3) can be rewritten in terms of the energy and pressure,

$$P = T\frac{\partial P}{\partial T} + \rho^2 \frac{\partial E}{\partial \rho}. \tag{4}$$

Satisfaction of Maxwell's relation ensures that there is at least one Helmholtz free-energy surface capable of providing the given energies and pressures. The work of Ref. [30] showed in the context of hydrodynamic simulations, a failure to ensure this level of consistency can lead to an effective error accumulation causing a divergence from the expected result with a consistent EOS.

Gibbs-Duhem relation: Due to the homogeneous first order property of the Helmholtz free-energy, the quantities P, T, and chemical potential μ are not independent of one another [41]. The relation between these quantities is referred to as the Gibbs-Duhem relation which states,

$$d\mu = -SdT + \frac{1}{\rho}dP. \tag{5}$$

Any interpolation scheme capable of providing chemical potentials must do so in a way that the gradients of the chemical potential are consistent with the entropy and density.

Stability conditions: As the temperature-density conditions of polystyrene data set cover only a single phase, the extremum principle (maximum entropy and minimum energy) must apply. In accordance, the Helmholtz free-energy must then be concave in temperature and convex in density [30,31,35,41],

$$\frac{\partial^2 F}{\partial T^2} \leq 0, \quad \rho^2 \frac{\partial}{\partial \rho}\left(\rho^2 \frac{\partial F}{\partial \rho}\right) \geq 0. \tag{6}$$

In terms of the energy and pressure the stability requirements of Eq. (6) become

$$\frac{\partial E}{\partial T} \geq 0 \quad \frac{\partial P}{\partial \rho} \geq 0. \tag{7}$$

If the energies and pressures provided by an interpolation scheme for a single phase away from critical points do not satisfy the conditions of Eq. (7) then they are not physically achievable by the system.

Section IV: Model construction

Transformation of the Helmholtz free-energy: Directly modeling the Helmholtz free-energy and utilizing Eqs. (1) and (2) has the advantage of ensuring Maxwell's relation is satisfied by construction. This approach has been shown to be successful in recent ML based EOS models [35,36,39] and will be the approach taken here. It is important to note, while the Helmholtz free-energies are not available in the polystyrene data set, it will be shown that the energies and pressures can be used to implicitly learn the Helmholtz free-energy. Furthermore, with the wide range of energies, pressures and temperatures encountered in the polystyrene data set it would be advantageous to work within a log representation of the Helmholtz free-energy. To accomplish this an auxiliary function f is introduced which will be related to the Helmholtz free-energy through an arcsinh transformation,

$$f = \operatorname{arcsinh}(F) = \ln\left(F + \sqrt{F^2 + 1}\right). \tag{8}$$

The use of arcsinh over a standard natural log eliminates the need for an arbitrary energy shift preventing any issues from arising due to a negative Helmholtz free-energy (without explicit values of F an arbitrary energy shift cannot guarantee positive values of F at all conditions).

For an input quantity X, the corresponding derivative of the Helmholtz free-energy transforms as,

$$X\frac{\partial F}{\partial X} = \cosh(f)\frac{\partial f}{\partial \ln(X)}. \tag{9}$$

Utilizing Eq. (9), the equations for the energy and pressure become

$$E = F - T\frac{\partial F}{\partial T} = \sinh(f) - \cosh(f)\frac{\partial f}{\partial \tau} \tag{10}$$

and

$$P = \rho^2\frac{\partial F}{\partial \rho} = \rho\cosh(f)\frac{\partial f}{\partial \sigma}. \tag{11}$$

Here, the quantities τ and σ are defined as $\tau = \ln(T)$ and $\sigma = \ln(\rho)$, respectively. They are to be considered as the input variables of f moving forward.

Eliminating the common factor of $\cosh(f)$ in Eqs. (10) and (11) leads to the following partial differential equation (PDE) that describes the auxiliary function f,

$$\frac{\partial f}{\partial \tau} + \rho\frac{E - \sinh(f)}{P}\frac{\partial f}{\partial \sigma} = 0. \tag{12}$$

If the energy and pressure are known as a function of temperature and density, Eq. (12) can be solved to determine f and correspondingly the Helmholtz free-energy of the system (similar method of solving PDE for unknown exchange-correlation free-energy by direct fitting of a suitable analytical form was used in Ref. [42]). As energy and pressure data are available at select temperatures and densities, this data can be used in conjunction with Eq. (12) during the training process to produce a physics informed ML model, which is capable of implicitly learning the Helmholtz free-energies as will be shown in the next sub-section.

Introducing ML: To utilize the transformed Helmholtz free-energy, the auxiliary quantity f will be modeled with an artificial neural network (ANN) [43]. That is, the ANN will take the quantities $\vec{x}^T = (\tau, \sigma)$ as an input and output a single value for the auxiliary function f. In this work a fully connected feedforward ANN with a single hidden layer is utilized. Mathematically, f can be written as

$$f^{ANN} = W^{(2)}g\left(W^{(1)}\vec{x} + \vec{\beta}\right). \tag{13}$$

Here, the matrices $W^{(1)}$, $W^{(2)}$ and the bias vector $\vec{\beta}$ contain free parameters that will be optimized during the training process. The function g is the activation function which was set to tanh throughout this work.

The parameters of the ANN are optimized by minimizing the following cost function,

$$C = \frac{1}{2\sum_i \gamma_i} \sum_i^{N_s} \gamma_i \left\{ \left(\frac{\partial f^{ANN}(\tau,\sigma)}{\partial \tau} + \rho_i^{ref} \frac{E_i^{ref} - \sinh\left(f^{ANN}(\tau,\sigma)\right)}{P_i^{ref}} \frac{\partial f^{ANN}(\tau,\sigma)}{\partial \sigma} \right)^2 \Bigg|_{\tau_i,\sigma_i} \right. \\ \left. + \lambda_1 \left(1 - \frac{E_i^{ANN}}{E_i^{ref}}\right)^2 + \lambda_2 \left(1 - \frac{P_i^{ANN}}{P_i^{ref}}\right)^2 \right\}. \quad (14)$$

The first term of the cost function is based on the PDE of Eq. (12). Here, the PDE is being evaluated at each training point, indexed by i, with the reference energy, pressure, temperature and density replacing the corresponding value. The gradients of the ANN needed in the first term of the cost function are calculated analytically,

$$\frac{\partial f^{ANN}}{\partial \vec{x}} = \begin{pmatrix} \frac{\partial f^{ANN}}{\partial \tau} \\ \frac{\partial f^{ANN}}{\partial \sigma} \end{pmatrix} = W^{(1)^T} W^{(2)^T} \circ g'\left(W^{(1)}\vec{x} + \vec{\beta}\right). \quad (15)$$

The symbol $\circ$ denotes a Hadamard product which in our notation is given higher priority than standard matrix multiplication in the order of operations. In effect, by minimizing the first term of the cost function the model aims to find the solution to Eq. (12). The second and third terms of the cost function, which contain the hyperparameters λ_1 and λ_2 respectively, are added to ensure that when the cost is minimized a trivial solution (f equal to a constant) of Eq. (12) is not found. Furthermore, γ_i is a stochastic quantity assigned to each member of the training set and can take on values of either 0 (probability 10%) or 1 (probability 90%). On each training epoch the value of γ_i for every training sample point is redrawn. This provides a level of stochasticity to the gradient descent to enable the model to work its way out of potential local minimum on the cost surface.

In principle, additional terms can be added to the cost function of Eq. (14) to enforce the remaining thermodynamic constraints. In practice however, this may lead to additional difficulties training the model. For instance, attempts were made to add a regularization term that penalized functions in the hypothesis set (set of functions represented by the architecture of the ANN) with negative entropy. This additional regularization often led to stability issues in the training process which can be attributed to such a term eliminating potential pathways in the domain of free parameters that the ANN can take during training. In effect, for ease of training it may be better to allow the ANN to pass through physically unacceptable functions for f on its way to the final thermodynamically consistent form.

Training the model: In total the reference data set is comprised of 198 temperature-density points where AIMD simulations were performed. Of these 198 points, 15 were randomly chosen and set aside for the test set. An additional 15 points were randomly chosen for the validation set which was used to monitor the training process to prevent overfitting. The remaining 168 points were then used as the training set. The temperature-density conditions chosen for each data set can be seen in Fig. 1a where each of the test, validation and training points are indicated by an x, a + and a filled circle respectively. Attempts to utilize a smaller fraction of the reference data demonstrated the training size could be cut to 90 data points and provide satisfactory results, see [45]. Below only results for the largest training set utilizing a single fold cross validation are discussed. Additional results with a 5-fold cross validation are comparable and can also be found in [45].

The number of nodes in the hidden layer of the ANN was set to 80. A value chosen to provide the ANN with reasonable flexibility while not exceeding a 2:1 ratio of free parameters to available training data. The free parameters were then optimized by performing a stochastic gradient descent [44] on the cost function of Eq. (14). During this procedure the gradients needed to update the weights were calculated analytically [45]. The hyperparameters λ_1 and λ_2 were both determined to be a value of 0.3. Tests of these hyperparameters indicated if the value was below 0.1 a trivial solution to Eq (12) was often found. Values above 1.0 would produce a model that fits the training data well but may have unphysical oscillations in the energies and pressures along the reference isochores. Furthermore, with a learning rate of 0.003 the training run consisted of 25 million epochs. Attempts to use a larger learning rate to shorten the training run often affected the stability of the stochastic gradient descent. The learning curves along with an analysis of the gradients during the backpropagation stage can be found in the supplemental material [45].

The code for the training of the PIML-EOS model was written from scratch in python version 3.6. NumPy [46] was utilized for all matrix operations as well as for its built-in hyperbolic trig functions. The mpi4pi library [47-50] was utilized to parallelize the training process. The python code for the PIML-EOS can be found at https://github.com/jhinz2/PIML-EOS.

Section V: Results and Discussion

Training results: The resulting relative errors in the predicted energies and pressures are shown in Fig. 1a and 1b respectively. These values have been tabulated and are presented in Table II. As can be seen, for both the energy and pressure 75% of the predictions are within 1% of the target value across all three data sets. In the case of energy, there were two points in the test set and nine points in the training set with a relative error above 5%, no points exceed a 25% error. Interestingly, all eleven of these points are clustered around the 10^6 K boundary where the energies of the KS and PIMC AIMD simulations were matched, Fig 1a. As there is both a higher uncertainty in the target energies and a likely discontinuity in the slope of the energies at the matching boundary, the struggles of the model here can be attributed to an underlying thermodynamic inconsistency in the reference data related to thermal exchange-correlation (XC) effects taken into account by the PIMC approach and missed by DFT simulations with

employment of a ground-state XC functional (see Ref. [51]). In the case of pressure, a similar result can be seen, Fig. 1b. While none of the predicted pressures exceeded a 5% error, the largest errors again occur at the matching boundary. However, unlike the energies, predicted pressures along the boundary of the domain of the reference data set also experience some of the larger errors.

Table II: Distribution of relative errors, in %, for the predicted energies and pressures of the PIML-EOS model on the training, validation and test sets. Here, the 25th, 50th and 75th percentiles of each distribution, measured from the left tail, are provided. Rows 1 and 2 are the model's predictions compared to the available AIMD data. Rows 3 and 4 are comparisons of the model's predictions to ideal gas (IG) values for temperatures above $3x10^7$ K. For clarity the percentiles should be interpreted as the fraction of each distribution which has an error below the given value. For example, 75% of the test predictions on AIMD data have an error less than 0.992%.

	Training					Validation					Test				
	min	25th	50th	75th	max	min	25th	50th	75th	max	min	25th	50th	75th	max
Energy	0.001	0.057	0.282	0.834	19.499	0.005	0.025	0.491	0.995	3.036	0.002	0.038	0.168	0.992	25.475
Pressure	0.001	0.289	0.553	0.910	4.948	0.020	0.402	0.570	0.848	1.744	0.015	0.362	0.587	0.974	3.122
IG energy											10^{-4}	0.594	1.042	1.500	1.800
IG pressure											10^{-5}	0.188	0.430	0.646	1.178

To examine the interpolations of the PIML-EOS model the energies and pressures were calculated at 900 temperature points (evenly spaced on the log scale) along each reference isochore. The results for energy are shown in Fig 2a and those for pressure are shown in Fig. 2b. Overall, the predictions of the PIML-EOS model appear smooth with no sharp jumps or oscillations. Even near the 10^6 K matching boundary where the prediction errors are largest the model is able to make a smooth transition from the DFT data to the PIMC data (more on this below). In the case of the 4.72 g/cm^3 isochore only high temperature data was available to the model. At lower temperatures the PIML-EOS model produces the remainder of the energies and pressures in a way that is consistent with the behavior of the neighboring reference isochores.

The smoothness of the interpolations is further confirmed by examining the derivatives of the PIML-EOS model. For both energy and pressure, the derivative with respect to temperature at each of the 900 points along the reference isochores are calculated analytically [45]. From Fig. 2c and 2d, it is clear both the derivative of the energy and the derivative of pressure with respect to temperature are continuous everywhere and appear to be smooth themselves. Around 10^6 K there does not appear to be any discontinuities or significant jumps associated with inconsistency of the slopes of the DFT and PIMC data. However, at present it is not possible with the available data to confirm whether the accuracy of predicted quantities such as specific heats in this region is significantly affected. Regardless, the smoothing of the discontinuity in the slope of the reference data can be advantageous for hydrodynamic simulations as discontinuities in the EOS

can cause numerical difficulties [30]. Furthermore, boundary effects at the high and low temperature regimes appear to be more prevalent in the model's derivatives than the predicted energies and pressures.

While the initial results of the model are promising, due to the limited availability of reference data it is important to provide further quantification of the generalization error. This validation can be carried out in the high temperature regime, $T > 3x10^7$ K, as the ground truth EOS from the MD simulations converges with that of an ideal gas (IG). To form this second test set 120000 IG energies and pressures are generated at temperature between $3x10^7$ and 10^8 K (evenly spaced on a log scale) and across the full range of densities considered. The PIML-EOS model trained only on the AIMD data is then applied to make corresponding predictions at each of these points. The resulting error distributions are provided in Table II. As can be seen, in the case of pressure the predictions are consistently within 1% of the IG values and never exceed an error of 1.2%. The errors in energy are slightly worse as the median error is just over 1% and the maximum error sits at 1.8%. This higher error observed in the energies can be attributed to small oscillations that appear along isotherms in this temperature regime. These oscillations suggest that a function that is constant in density, as the ground truth EOS is in this regime, may be just outside of the hypothesis set formed by the ANN (analogous to expanding a constant function in a finite number of sines and cosines). Overall, based on this result, the results of the original test set and the observed behavior of the interpolations, it is expected that the general error of the model across the full domain of temperature and densities considered will be around 1% for both the energy and pressure.

Consistency checks: To evaluate Maxwell's relation the energy, pressure and the corresponding derivatives from the PIML-EOS model were calculated at 90000 temperature and density points (evenly space on log scale) across the same domain of temperature and density consistent with the reference data set. The residual error, defined as the absolute value of the difference between both sides of Eq. (4), was calculated at each point and the resulting distribution has been tabulated in Table III. As can be seen, the errors in Maxwell's relation are at or near machine precision confirming Maxwell's relation holds.

To determine if the non-negativity condition on the pressure and the conditions of stability are satisfied, the maximum between 0 and the negative of the predicted target quantity of interest was evaluated at each of the 90000 points used above in the test of the Maxwell relation. The resulting distributions, as shown in Table III, indicate there are no points where the pressure becomes negative and that the stability conditions of Eq. (7) hold across the domain of temperatures and densities consistent with the reference data set. However, as a note of caution, care must be taken when the predictions of the PIML-EOS model are extrapolated beyond the domain containing the reference data. As can be seen in Fig. 2c, at temperatures below $5x10^3$ K the stability condition for the energy begins to break down.

Table III: Distributions for various checks on the thermodynamic consistency of the PIML-EOS model. Column one indicates the quantity calculated at each of the 90000 points sampled across the domain of T and ρ consistent with the reference data. For Maxwell's relation this is the absolute value of the difference between the two sides of Eq. (4). Column two gives the

minimum of each distribution, Columns three through five indicate the 25th, 50th and 75th percentile of the distribution respectively; and column six provides the maximum of the distribution.

Distribution	min	25th	50th	75$^{t\,h}$	max
Maxwell relation	0.0	0.0	$2.22\text{x}10^{-16}$	$7.11\text{x}10^{-15}$	$2.73\text{x}10^{-12}$
$\max(0,-P)$	0.0	0.0	0.0	0.0	0.0
$\max\left(0,-\frac{\partial E}{\partial T}\right)$	0.0	0.0	0.0	0.0	0.0
$\max\left(0,-\frac{\partial P}{\partial \rho}\right)$	0.0	0.0	0.0	0.0	0.0

Next, for the evaluation of the Gibbs-Duhem relation the chemical potential from the PIML-EOS model was obtained using the following Euler equation,

$$\mu = F + \frac{1}{\rho}P. \tag{16}$$

Eq. (16) comes from a manipulation of Eq. (1) where the Euler relation $E = ST + \mu - P/\rho$ has been utilized. As the chemical potential is needed as a function of pressure and not density, Eq. (5), a transformation of the input variables is performed. This is done by fitting a tangent plane to the chemical potential surface at each of the 90000 temperature-density points. For each fit, both the temperature and density were varied by ± 0.05% to generate 25 points around (T_0, ρ_0), the conditions where the Gibbs-Duhem relation is being evaluated. Using a least squares fit to the model predictions at these 25 conditions the coefficients a_1 and a_2 in the tangent plane

$$\mu - \mu_0 = a_1(T - T_0) + a_2(P - P_0) \tag{17}$$

where optimized. Here, (P_0, μ_0) are the predicted values of the pressure and chemical potential at (T_0, ρ_0). The coefficients associated with these fits are directly related to the derivatives of the chemical potential and can be interpreted as

$$a_1 = \frac{\partial \mu}{\partial T}, \qquad a_2 = \frac{\partial \mu}{\partial P}. \tag{18}$$

Comparing Eq. (5) and Eq. (18), the coefficients a_1 and a_2 should be equal to the negative of the entropy and the reciprocal of the density respectively. Here, the entropy is calculated from the Helmholtz free-energy and the comparison to the coefficient a_1 is made in Fig. 3a. Overall, the relative error in a_1 is consistently below 1% across most of the domain associated with the reference data. Near the matching boundary, 10^6 K, there are some instances where this error can reach 10% or more. In total, these high error points constitute only 300 of the 90000 points sampled. Furthermore, the coefficient a_2 is compared to the reciprocal of the

density in Fig 3b. Again, the error in the coefficient is consistently below 1% for most conditions sampled with the exception of a few points near the matching boundary. For both coefficients, the high error points seem to be the most sensitive to the window used to fit the tangent plane. With a more accurate scheme to calculate the derivatives of the chemical potential these larger errors may be reduced. Overall, these results demonstrate the Gibbs-Duhem relation holds for the PIML-EOS model but may be susceptible to a breakdown in regions where thermodynamic inconsistencies exist in the reference data.

The remaining consistency check is to examine the sign of the model's predicted entropy. As with the pressure and stability conditions, the maximum of 0 and the negative of the entropy is calculated at each of the 90000 points sampled. The resulting color map of values can be seen in Fig. 4a. Below 20000 K for most densities considered the entropy becomes negative which is the first observed thermodynamic inconsistency in the PIML-EOS model's predictions not related to an inconsistency in the reference data.

This inconsistency in the entropy can be explained by the fact that the use of $E(T,\rho)$ and $P(T,\rho)$ does not provide the same information as $F(T,\rho)$ about a system's EOS. This means the true Helmholtz free-energy of polystyrene differs by some unknown function of temperature and density from the Helmholtz free-energy of the model,

$$F^{sys} = F^{ANN} + h(T,\rho). \tag{19}$$

The form of the function h can be determined by the fact that both the pressure and energy used in the construction of the model are total quantities containing all contributions, both electronic and ionic, within the context of the approximations made in the AIMD simulations. As such the function h is constrained by $P^{sys} = P^{ANN}$ and $E^{sys} = E^{ANN}$.

Plugging Eq. (19) into Eq. (2) and enforcing the constraint on pressure, it can be seen that the function h will be independent of density, $h(\rho,T) \rightarrow h(T)$. In a similar manner, Eq. (19) can be inserted into Eq. (1) and the constraint on the energy can be applied. This results in the following ordinary differential equation that describes h,

$$h(T) - T\frac{dh(T)}{dT} = 0. \tag{20}$$

Solving Eq. (20) leads to h being a linear function of temperature. Therefore, during the training process the PIML-EOS model picks out one Helmholtz free-energy surface in a family of possible surfaces with the resulting true Helmholtz free-energy of the system being

$$F^{sys} = F^{ANN} - S_0 T. \tag{21}$$

The unknown constant S_0 can be determined with an exact calculation of the system's entropy at a single temperature-density point or in the limit where the Helmholtz free-energy goes to a known form. It's important to note, the presence of this unknown constant does not affect the previous consistency checks as the constant will either cancel out or be eliminated by a derivative. It is also of note that any model that learns the Helmholtz free-energy from only energy and pressure data will be missing this linear contribution of temperature.

To determine the constant S_o for the polystyrene data set the convergence to an IG in the high temperature regime (see Fig 2) is utilized. Here, F^{sys} in Eq. (21) is replaced with the exact expression for an IG, F^{IG} [41], and the difference $\Delta F = F^{IG} - F^{ANN}$ is taken at each of the 90000 conditions previously sampled. From the distribution of $\Delta F/T$, Fig. 4b, all points with a temperature greater than $3\text{x}10^7$ K were averaged producing a value of 22.24 for S_0. The corresponding standard deviation associated with this average is 0.04 confirming that $\Delta F/T$ does in fact go to a constant at high temperatures. When S_0 is added to the predicted entropies from the PIML-EOS model, the thermodynamic inconsistency is resolved as shown in Fig 4c. With the calculation of S_0 the total Helmholtz free-energy is now completely determined enabling the prediction of quantities such as the total entropy and total chemical potential of the system at all temperature-density conditions. As these quantities are not directly obtainable from AIMD simulations, this makes the PIML-EOS model a valuable tool for the construction of a more complete EOS table and may help facilitate a better understanding of material properties.

Additional validation: With the consistency checks complete, two additional tests of the model are performed. For the first test, the PIML-EOS model was used to calculate the principle Hugoniot which describes the locus of possible final states, (E_2, P_2, ρ_2), a system can achieve after being shock compressed from an initial state (E_1, P_1, ρ_1). This locus of final states is determined by the Rankine-Hugoniot equation,

$$E_2 - E_1 + \frac{1}{2}(P_2 + P_1)\left(\frac{1}{\rho_2} - \frac{1}{\rho_1}\right) = 0. \tag{22}$$

For the calculation of the polystyrene Hugoniot the same initial conditions used by Zhang *et al* [29] are used here. In dimensionless quantities these values are $E_1 = -10.4281$, $P_1 = 0$ and $\rho_1 = 0.5$. The resulting Hugoniot, Fig 5, is in overall good agreement with that produced by Zhang *et al* with a cubic spline interpolation. The maximum compression of both curves is within 0.5% of one another. In the high-pressure regime oscillations in the PIML-EOS predicted Hugoniot of ± 2% about the Zhang *et al* curve can be observed. This can be attributed to the Hugoniot's sensitivity to errors in the fitted EOS and not the presence of apparent shell structure as retraining the model often resulted in a differing behavior of the oscillations. The use of an ensemble approach has been shown to eliminate such oscillations [38] and was attempted in the supplemental material [45]. It was found that the behavior of the Hugoniot, particularly in the low-pressure regime, is highly sensitive to errors in the model. Therefore, caution must be taken when interpreting the Hugoniot through a physics lens.

For the second additional test, a transformation to the energy representation, $E(S, \rho)$, is performed. As was done in the test of the Gibbs-Duhem relation, the transformation of the input variables is done by fitting a tangent plane at each of the 90000 temperature-density conditions previously used in the consistency checks. The coefficients of the fits are then compared to the expected values of the derivatives $\partial E/\partial S = T$ and $\partial E/\partial \rho = -P/\rho$. From Figs. 3c and 3d it can be seen that the derivatives are reproduced well within a 1% error. Together with the tests of the Gibbs-Duhem relations, this demonstrates the PIML-EOS model can be trained in one thermodynamic potential and utilized in another.

Section VI: Conclusion

In summary, a physics informed machine learning EOS model was constructed such that energy and pressure data can be utilized to implicitly learn the Helmholtz free-energy up to an unknown constant. With the use of a known limit, the unknown constant can be determined allowing for previously unobtainable quantities such as the total Helmholtz free-energy, entropy and chemical potential to be calculated for AIMD based EOS tables. Trained on reference data for warm dense polystyrene, the PIML-EOS model was capable of reproducing the target energies and pressures within a 1% error. The model was also shown to be thermodynamically consistent, providing thermodynamically stable predictions that satisfied both the Maxwell and the Gibbs-Duhem relations. Furthermore, we found that the model appears to be capable of identifying inconsistencies in the reference data set. While this is not the intended purpose of the model, this sensitivity may be a valuable tool to improve existing discrete EOS tables. Moving forward, additional tests are needed to determine how the model will handle more complex systems that experience a phase transition in the considered domain of temperature and density. At present, it appears such transitions will likely be smoothed out which could be advantageous for hydrodynamic simulations; but for other applications where smoothing is undesirable, further developments of the model are likely needed. Furthermore, additional validation should be performed, when possible, to ensure the level of error on the energies and pressures is maintained for quantities such as specific heats.

Supplementary Material

The supplemental material contains technical details about the implementation of the PIML-EOS model. This include details about how gradients of the model are calculated for both the backpropagation and analysis of the smoothness of the energies and pressures. Additionally, learning curves from the training runs can be found here.

Acknowledgement

J. H., V. V. K., D. I. M. and S. X. H. were supported by the Department of Energy National Nuclear Security Administration under Award Number DE-NA0003856, the University of Rochester, the New York State Energy Research and Development Authority, and U.S. National Science Foundation PHY Grant No. 2205521. Partial funding for S. X. H. was provided by the NSF Physics Frontier Center Award PHY-2020249. All computations were performed on the Laboratory for Laser Energetics HPC systems.

Conflict of interest

The authors have no conflict of interests.

Author contributions

J. Hinz: Conceptualization (equal); methodology (lead); software (lead); writing – original draft (lead); writing – review and editing (equal). **Dayou Yu**: Conceptualization (equal); methodology (supporting); writing - review and editing (supporting). **Deep Shankar Pandey**:

Conceptualization (equal); methodology (supporting); writing - review and editing (supporting). **Hitesh Sapkota**: Conceptualization (supporting); methodology (supporting). **Qi Yu**: Conceptualization (lead); methodology (equal); supervision (equal); writing – review and editing (equal). **D. I. Mihaylov**: Conceptualization (equal); methodology (equal); writing – review and editing (supporting). **V. V. Karasiev**: Conceptualization (lead); methodology (equal); supervision (lead); writing – review and editing (equal). S. X. Hu: Conceptualization (lead); methodology (equal); supervision (lead); writing – review and editing (equal).

Data Availability

The data that supports the findings of this study are openly available in the database constructed in Ref. [28] under the table C18H18_EOS_09-18-20.txt.

Disclaimer

References

1. Y. Komatsu, T. Sasaki, T. Kikuchi, N. Harada and H. Nagatomo, "Changes of implosion dynamics derived by difference of equation of state," EPJ Web of Conferences **59**, 04010 (2013).
2. S. Fiak, A. Tauschwitz, and I. Iosilevskiy, "The equation of state package FEOS for high energy density matter," Comput. Phys. Commun. **227**, 117-125 (2018).
3. M. Zeman, M. Holec, and P. Váchal, "HerEOS: A framework for consistent treatment of the Equation of State in ALE hydrodynamics," Comput. Math. With Appl. **78**, 483-503 (2019).
4. S. X. Hu, B. Militzer, V. N. Goncharov, and S. Skupsky, "First-principles equation-of-state table of deuterium for inertial confinement fusion applications," Phys. Rev. B **84**, 224109 (2011).
5. M. A. Morales, L. X. Benedict, D. S. Clarka, E. Schwegler, I. Tamblyn, S. A. Bonev, A. A. Correa, and S. W. Haan, "Ab initio calculations of the equation of state of hydrogen in a regime relevant for inertial fusion applications," High Energy Density Phys. **8**, 5-12 (2012).
6. S. X. Hu, R. Gao, Y. Ding, L. A. Collins, and J. D. Kress, "First-principles equation-of-state table of silicon and its effects on high-energy-density plasma simulations," Phys. Rev. E **95**, 043210 (2017).

7. S. X. Hu, L. A. Collins, V. N. Goncharov, J. D. Kress, R. L. McCrory, and S. Skupsky, "First-principles equation of state of polystyrene and its effect on inertial confinement fusion implosions," Phys. Rev. E **92**, 043104 (2015).
8. Y. H. Ding and S. X. Hu, "First-principles equation-of-state table of beryllium based on density-functional theory calculations," Phys. Plasmas **24**, 062702 (2017).
9. P. M. Celliers, M. Millot, S. Brygoo, R. S. McWilliams, D. E. Fratanduono, J. R. Rygg, A. F. Goncharov, P. Loubeyre, J. H. Eggert, J. L. Peterson, *et al*, "Insulator-metal transition in dense fluid deuterium," Science **361**, 677-682 (2018).
10. M. D. Knudson, M. P. Desjarlais, A. Becker, R. W. Lemke, K. R. Cochrane, M. E. Savage, D. E. Bliss, T. R. Mattsson, R. Redmer, "Direct observation of an abrupt insulator-to-metal transition in dense liquid deuterium," Science **348**, 1455-1460 (2015).
11. Y. Shimoni, O. Aharonson, and R. Rufu, "The influence of equation of state on impact dynamics between Pluto-like bodies," Icarus **371**, 114677 (2022).
12. R. Püstow, N. Nettelmann, W. Lorenzen, and R. Redmer, "H/He demixing and the cooling behavior of Saturn," Icarus **267**, 323-333 (2016).
13. N. Nettelmann, A. Becker, B. Holst, and R. Redmer, "JUPITER MODELS WITH IMPROVED AB INITIO HYDROGEN EQUATION OF STATE (H-REOS.2)," ApJ **750**, 52 (2012).
14. N. Nettelmann, R. Püstow, and R. Redmer, "Saturn layered structure and homogeneous evolution models with different EOSs," Icarus **225** 548-557 (2013).
15. Ø. Wilhelmsen, A. Aasen, G. Skaugen, P. Aursand, A. Austegard, E. Aursand, M. Aa. Gjennestad, H. Lund, G. Linga, and M. Hammer, "Thermodynamic Modeling with Equations of State: Present Challenges with Established Methods," Ind. Eng. Chem. Res. **56**, 3503−3515 (2017).
16. O. Kunz and W. Wagner, "The GERG-2008 Wide-Range Equation of State for Natural Gases and Other Mixtures: An Expansion of GERG-2004," J. Chem. Eng. Data **57**, 3032−3091 (2012).
17. J. Gernert, A. Jager, and R. Span, "Calculation of phase equilibria for multi-component mixtures using highly accurate Helmholtz energy equations of state," Fluid Phase Equilib. **375**, 209-218 (2014).
18. N. Kukreja, P. Ghoderao, V. H. Dalvi, and M. Narayan, "Cubic equation of state as a quartic in disguise," Fluid Phase Equilib. **531**, 112908 (2021).
19. S. P. Lyon and J. D. Johnson, "SESAME: The Los Alamos National Laboratory equation of state database," Tech. Rep. LA-UR-92-3407, Los Alamos National Laboratory, Los Alamos, NM, USA, 1992.
20. K. A. Velizhanin and J. D. Coe, "Automated fitting of Semi-empirical multiphase equation of state for carbon," AIP Conf. Proc. **2272**, 070051 (2020).
21. Y. L. Guennec, R. Privat, S. Lasala, J. N. Jaubert, "On the imperative need to use a consistent a-function for the prediction of pure-compound supercritical properties with a cubic equation of state," Fluid Phase Equilib. **445**, 45-53 (2017).
22. M. A. Barrios, T. R. Boehly, D. E. Fratanduono, J. H. Eggert, G. W. Coliins, and D. D. Meyerhofer, "Precision equation-of-state measurements on National Ignition Facility

ablator materials from 1 to 12 Mbar using laser-driven shock waves," J. Appl. Phys. **111**, 093515 (2012).
23. J. Li, Q. Wu, J. Li, T. Xue, Y. Tan, X. Zhou, Y. Zhang, Z. Xiong, Z. Gao, and T. Sekine, "Shock melting curve of iron: A consensus on the temperature at the Earth's inner core boundary," Geophys. Res. Lett. **47**, e2020GL087758 (2020).
24. L. E. Crandall, J. R. Rygg, D. K. Spaulding, T. R. Boehly, S. Brygoo, P. M. Celliers, J. H, Eggert, D. E. Fratanduono, B. J. Henderson, M. F. Huff, *et al*, "Equation of State of CO2 Shock Compressed to 1 TPa," Phys. Rev. Lett. **125**, 165701 (2020).
25. H. Shu, Y. Zhang, B. Wang, W. Yang, H. Dong, T. Tobase, J. Ye, X. Huang, S. Fu, Q. Zhou, and T. Sekine, Laser-shocked calcium difluoride (CaF2) as a warm dense matter," Phys. Plasmas 27, 030701 (2020).
26. R. M. More, K. H. Warren, D. A. Young, and G. B. Zimmerman, "A new quotidian equation of state (QEOS) for hot dense matter," Phys. Fluids **31**, 3059–3078 (1988).
27. R. P. Feynman, N. Metropolis, and E. Teller, "Equations of state of elements based on the generalized Fermi-Thomas theory," Phys. Rev. **75**, 1561 (1949).
28. B. Militzer, F. Gonzalez-Cataldo, S. Zhang, K. P. Driver, and F. Soubiran, "First-principles equation of state database for warm dense matter computation," Phys. Rev. E **103**, 013203 (2021).
29. S. Zhang, K. P. Driver, F. Soubiran, and B. Militzer, "First-principles equation of state and shock compression predictions of warm dense hydrocarbons," Phys. Rev. E **96**, 013204 (2017).
30. F. D. Swesty, "Thermodynamically Consistent Interpolation for Equation of State," J. Comput. Phys. **127**, 118-127 (1996).
31. G. A. Dilts, "Consistent thermodynamic derivative estimates for tabular equations of state," Phys. Rev. E **73**, 066704 (2006).
32. A. Carranza-Abaid, H. F. Svendsen, and J. P. Jakobsen, "Thermodynamically consistent vapor-liquid equilibrium modeling with artificial neural networks," Fluid Phase Equilib. **564**, 113597 (2023).
33. K. L. Mentzer and J. L. Peterson, "Neural network surrogate models for equations of state," Phys. Plasmas **30**, 032704 (2023).
34. R. G. Patel, I. Manickam, N. A. Trask, M. A. Wood, M. Lee, I. Tomas, and E. C. Cyr, "Thermodynamically consistent physics informed neural network for hyperbolic systems," J. Comput. Phys. **449**, 110754 (2022).
35. D. Rosenberger, K. Barros, and T. C. Germann, "Machine learning of consistent thermodynamic models using automatic differentiation," Phys. Rev. E **105**, 045301 (2022).
36. G. Chaparro and E. A. Muller, "Development of thermodynamically consistent machine-learning equations of state: Application to the Mie fluid," J. Chem. Phys. **158**, 184505 (2023).
37. G. Truc, N. Rahmanian, and M. Pishnamazi, "Assessment of Cubic Equations of State: Machine Learning for Rich Carbon-Dioxide Systems," Sustainability **13**, 2527 (2021).
38. D. Yu, *et al*, "Deep Energy-Pressure Regression for a Thermodynamically Consistent EOS Model," Mach. Learn.: Sci. Technol. **5**, 015031 (2024).

39. J. A. Gaffney, L. Yang, and S. Ali, “Constraining model uncertainty in plasma equation-of-state models with a physics-constrained Gaussian process,” arXiv:2207.00668 (2022).
40. K. Zhu and E. A. Muller, “Generating a Machine-Learned Equation of State for Fluid Properties,” J. Phys. Chem. B **124**, 8628−8639 (2020).
41. H. B. Callen, “Thermodynamics and an introduction to thermostatistics,” Wiley, 2nd edition, 1985, pg. 37, 60, 146, 155, 182, 208, 373.
42. V. V. Karasiev, T. Sjostrom, J. Duffy, and S. B. Trickey, “Accurate Homogeneous Electron Gas Excange-Correlation Free Energy for Local Spin-Density Calculations”, Phys. Rev. Lett. **112**, 076403 (2014).
43. W. S. McCulloch and W. Pitts, “A logical calculus of the ideas immanent in nervous activity,” Bull. Math. Biophys. **5**, 115–133 (1943).
44. J. Kiefer and J. Wolfowitz, “Stochastic Estimation of the Maximum of a Regression Function,” Ann. Math. Statist. **23**, 462-466 (1952).
45. Supplemental material
46. C. R. Harris, K. J. Millman, S. J. van der Walt, R. Gommers, P. Virtanen, D. Cournapeau, E. Wieser, J. Taylor, S. Berg, N. J. Smith, et al., “Array programming with NumPy,” Nature **585**, 357 (2020).
47. L. Dalcín, R. Paz, and M. Storti, “MPI for Python,” J. Parallel Distrib. Comput. **65**, 1108 (2005).
48. L. Dalcín, R. Paz, M. Storti, and J. D’Elía, “MPI for Python: Performance improvements and MPI-2 extensions,” J. Parallel Distrib. Comput. **68**, 655 (2008).
49. L. D. Dalcin, R. R. Paz, P. A. Kler, and A. Cosimo, “Parallel distributed computing using Python,” Adv. Water Resour. **34**, 1124 (2011).
50. L. Dalcin and Y. L. L. Fang, “Mpi4py: Status update after 12 years of development,” Comput. Sci. Eng. **23**, 47 (2021).
51. V. V. Karasiev, D. I. Milhaylov, S. X. Hu, “Meta-GGA exchange-correlation free energy density functional to increase the accuracy of warm dense matter simulations”, Phys. Rev. B **105**, L081109 (2022).

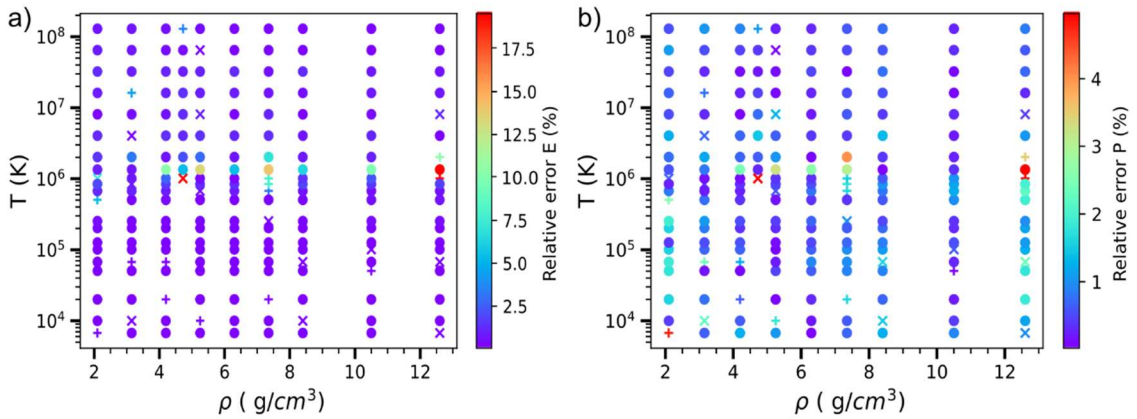

Figure 1: Prediction errors for the energy a) and pressure b). Filled circles, pluses and x's represent points in the training, validation and test set respectively. The color bar is with respect to the relative error, in %, for each quantity. Note, for temperature and density the conversion back to dimensional variables has been made.

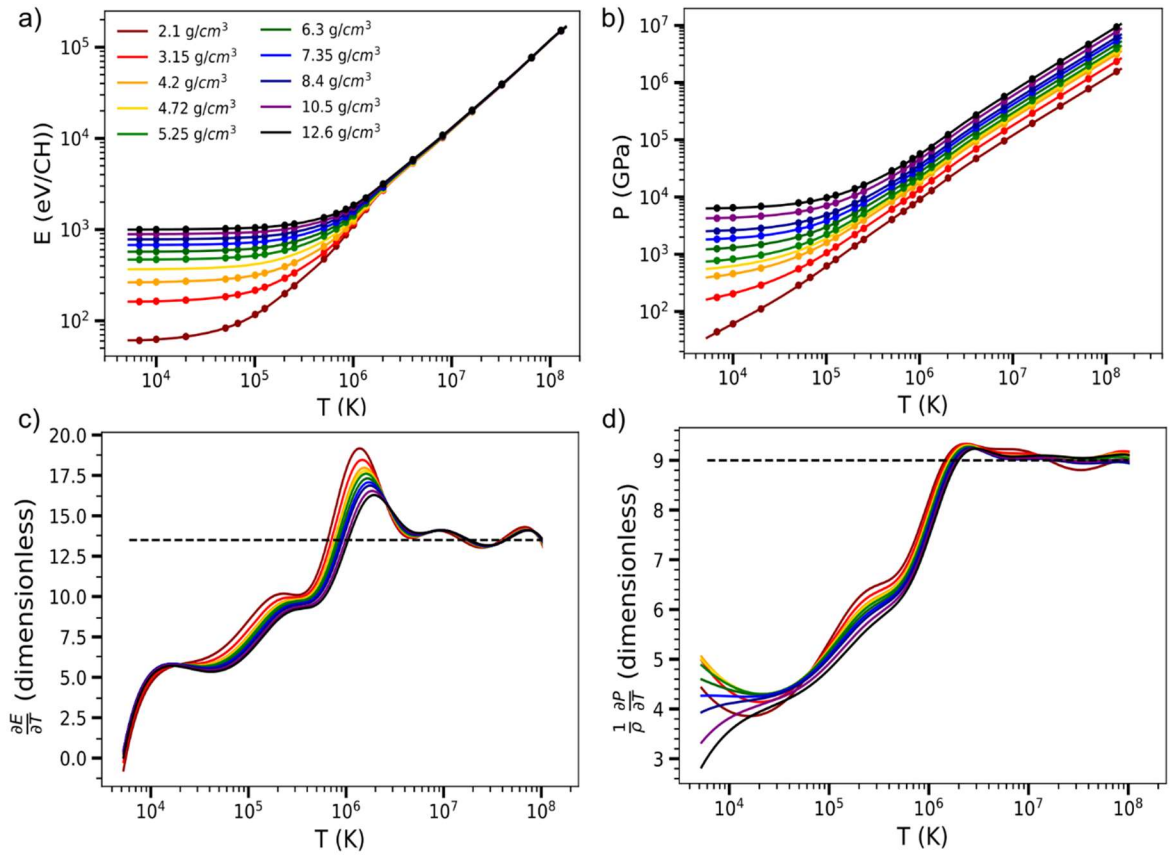

Figure 2: a) interpolated energies and b) interpolated pressures with the PIML-EOS model along the reference isochores. Solid lines indicate the model's predictions while circles indicate the reference data points. Note, the energies have been shifted for plotting purposes. The energies of 2.1 g/cm³ isochore have been shifted by 1100 eV/CH and each subsequent isochore has been shifted by an additional 100 eV/CH. c) and d) provide the derivative of the energy and pressure with respect to temperature, respectively, from the model along each of the reference isochores. The dotted black line indicates the expected value for an ideal gas. Note, for temperature, density, energy and pressure the conversion back to dimensional variables has been made. Derivatives have been intentionally left dimensionless to provide insight into the number of degrees of freedom in the system.

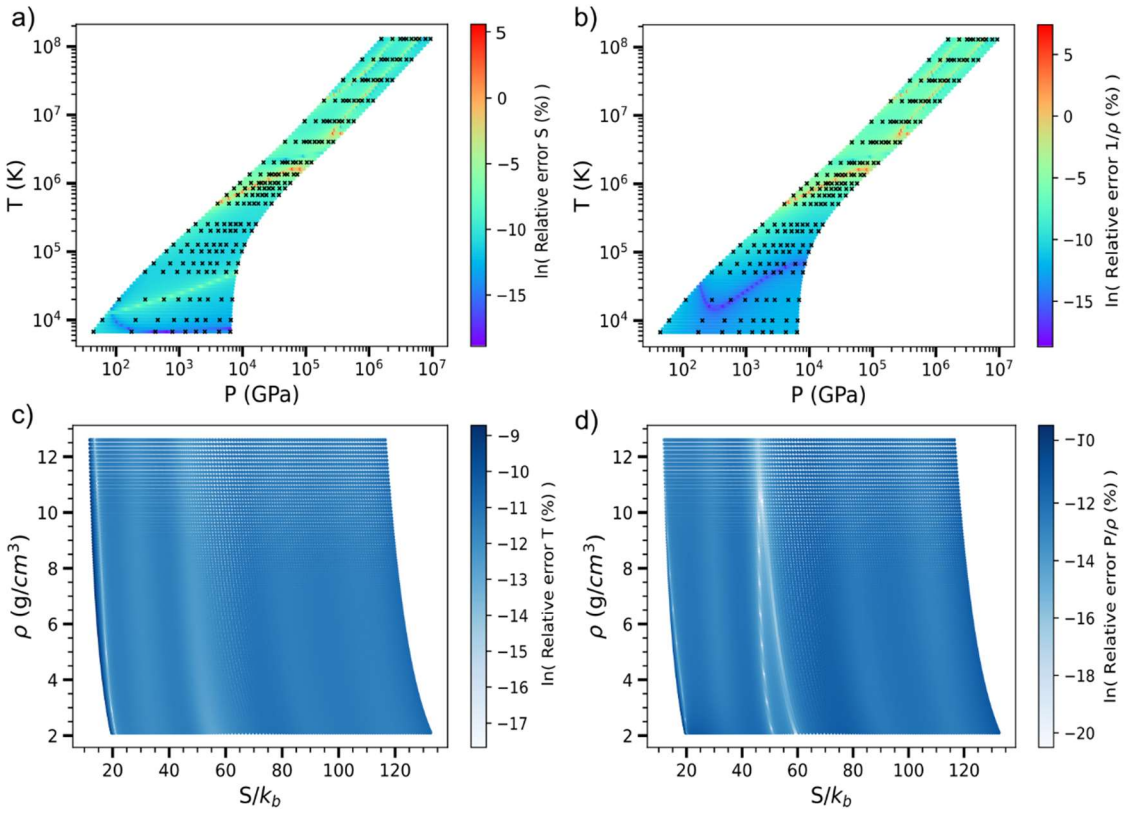

Figure 3: a) and b) indicate the error in the calculated gradients $\partial\mu/\partial T$ and $\partial\mu/\partial P$, respectively, needed in the evaluation of the Gibbs-Duhem relation. The color bar is based on the log of the relative error in %. The black circles are the reference data. c) and d) provide the error on the gradients $\partial E/\partial S$ and $\partial E/\partial\rho$ respectively when the model is transformed to the energy representation $E(S,\rho)$. Note, for temperature, density and pressure the conversion back to dimensional variables has been made.

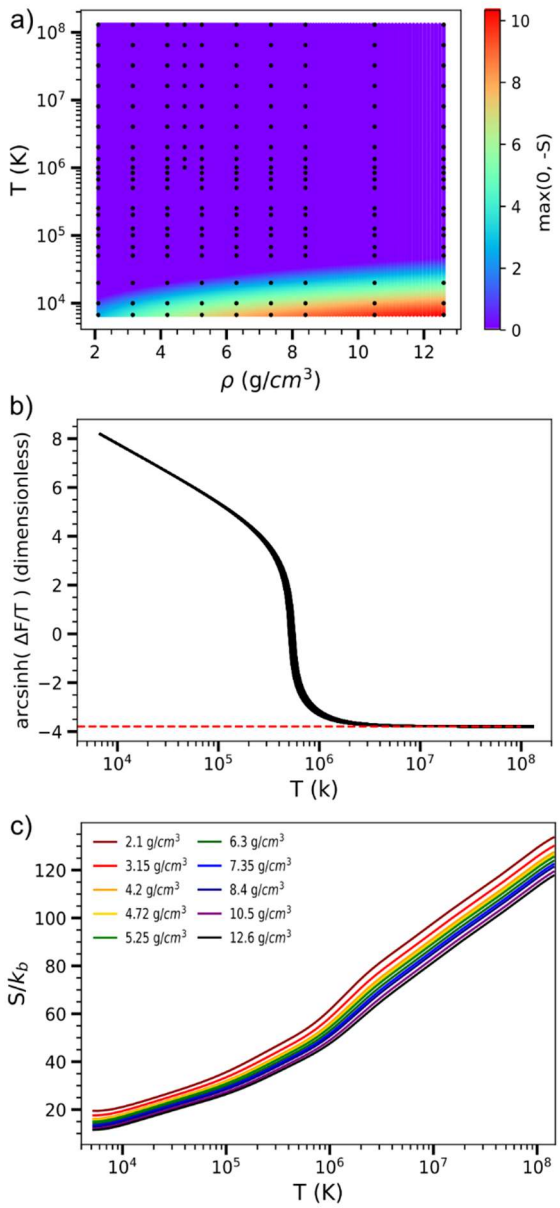

Figure 4: a) evaluation of the sign of the predicted entropy across the domain of thermodynamic conditions consistent with the reference data which is indicated by the black circles. b) distribution of $\Delta F/T$ for the comparison with an ideal gas. The red dotted line indicates the values of S_0 needed to completely determine the total Helmholtz free-energy of the system. c) Corrected entropy along each of the reference isochores.

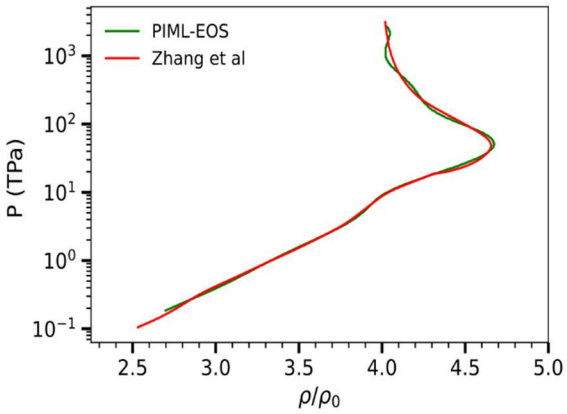

Figure 5: Calculated Hugoniot for the PIML-EOS model, green curve. A comparison is made to the result predicted by Zhang et al [29], red curve, which was obtained with a cubic spline interpolation of the reference data set.

Supplementary Material: "The development of thermodynamically-consistent and physics-informed equation-of-state model through machine learning"

J. Hinz[1], Dayou Yu[2], Deep Shankar Pandey[2], Hitesh Sapkota[2], Qi Yu[2], D. I. Mihaylov[1], V. V. Karasiev[1], and S. X. Hu[1,3,4]

[1]Laboratory for Laser Energetics, University of Rochester, Rochester NY, 14623
[2] Rochester Institute of Technology, Rochester NY, 14623
[3]Department of Physics and Astronomy, University of Rochester, Rochester NY, 14627
[4]Department of Mechanical Engineering, University of Rochester, Rochester NY, 14611

Section I: Overview

Here additional details about the PIML-EOS model can be found. In section II all quantities used throughout this document are defined. From there the gradients needed in the backpropagation used during the training process are constructed in section III. Section IV provides the analytical derivatives of the model's energy and pressure used in the analysis of the model. Results of stability can be found in section V and a 5-fold cross validation was performed in section VI.

Section II: Defining terms

Table I: Quantities, and their definitions/description, used throughout this document.

Quantity	Description
F, E, P, T, ρ	Helmholtz free-energy, energy, pressure, temperature and density respectively.
$W^{(1)}, W^{(2)}, \vec{\beta}$	Weight matrices and bias vector associated with the neural network
$\vec{x} = \begin{pmatrix} \tau \\ \sigma \end{pmatrix} = \begin{pmatrix} \ln T \\ \ln \rho \end{pmatrix}$	Input vector for the neural network.
$\vec{H}^{(i)} = W^{(1)}\vec{x}^{(i)} + \vec{\beta}$	Hidden layer of the neural network for input vector indexed by i.
$f_i^{ANN} = W^{(2)} g\left(\vec{H}^{(i)}\right)$	Auxiliary function modeled by a neural network with activation function g.
$\frac{\partial f^{ANN}}{\partial \vec{x}} = W^{(1)^T} W^{(2)^T} \circ g'\left(\vec{H}\right)$	Derivative of the neural network with respect to the input vector.
$\vec{a} = \begin{pmatrix} 1 \\ 0 \end{pmatrix}, \quad \vec{b} = \begin{pmatrix} 0 \\ 1 \end{pmatrix}$	Vectors utilized in the backpropagation.
$\vec{v}^{(i)} = \vec{a} + \left(\rho_i \frac{E_i^{ref} - \sinh\left(f_i^{ANN}\right)}{P_i^{ref}} \right) \vec{b}$	Vector quantity appearing in the gradients of the model.

$e_{1,i} = \frac{-2\lambda_1}{E_i^{ref}}\left(1 - \frac{E_i^{ANN}}{E_i^{ref}}\right)\cosh\left(f_i^{ANN}\right)$	Scaler quantity appearing in the gradients of the model.
$e_{2,i} = e_{1,i} + \sinh\left(f_i^{ANN}\right)\vec{a}^T \left.\frac{\partial f^{ANN}}{\partial \vec{x}}\right\|_{\vec{x}^{(i)}}$	Scaler quantity appearing in the gradients of the model.
$p_{1,i} = e_{1,i}(E \to P, \lambda_1 \to \lambda_2)$	Scaler quantity appearing in the gradients of the model. The argument denotes swapping out variables appearing in the previous quantity.
$p_{2,i} = e_{2,i}(E \to P, \lambda_1 \to \lambda_2)$	Scaler quantity appearing in the gradients of the model. The argument denotes swapping out variables appearing in the previous quantity.
$\vec{r}^{(i)} = -e_{1,i}\,\vec{a} + p_{1,i}\vec{b}$	Vector quantity appearing in the gradients of the model.

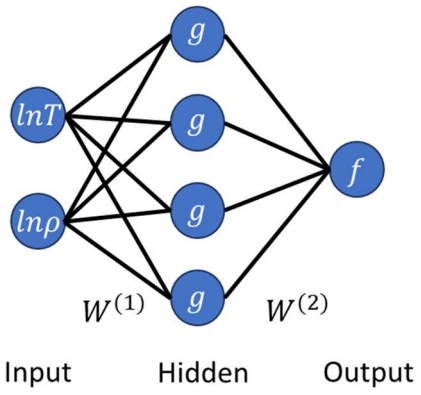

Figure S1: Form of the artificial neural network used in the PIML-EOS model.

Section III: Gradients of the cost function

The cost function used to train the PIML-EOS model consists of two pieces. The first contribution to the cost is based on the square residual error of the partial differential equation governing the auxiliary function f evaluated at each of the training points,

$$C_{pde} = \frac{1}{2N}\sum_i^{N_s} \gamma_i \left(\frac{\partial f^{ANN}}{\partial \tau} + \rho_i^{ref}\frac{E_i^{ref} - \sinh(f^{ANN})}{P_i^{ref}}\frac{\partial f^{ANN}}{\partial \sigma}\right)^2\Bigg|_{\tau_i,\sigma_i}. \quad (1)$$

Minimization of C_{pde} has the potential to produce either a trivial or nontrivial solution to the pde. To avoid the trivial solution an additional term based on the fractional error of the predicted energies and pressures is constructed,

$$C_0 = \frac{1}{2N}\sum_i^{N_s} \gamma_i \left\{ \lambda_1 \left(1 - \frac{E_i^{ANN}}{E_i^{ref}}\right)^2 + \lambda_2 \left(1 - \frac{P_i^{ANN}}{P_i^{ref}}\right)^2 \right\}. \quad (2)$$

Here, $\lambda_1$and λ_2 are hyperparameters of the cost function that must be optimized. Additionally, the quantity N_s is the total number of training points and $N = \sum \gamma_i$ is the number of training points used at each epoch with $\gamma_i \in \{0,1\}$ determining if a given training point contributes to the cost (and gradients). The total cost is then the sum of the two terms above.

The optimal weights and biases of the neural network are achieved when the total cost has been minimized. To carry out this minimization a stochastic gradient descent was performed. Here, the gradients are calculated analytically and are provided below in table II for reference.

Table II: Analytical form of the gradients of the cost function.

Gradient	Analytical form
$\frac{\partial C_{pde}}{\partial W^{(2)}}$	$\frac{1}{N}\sum_i^{N_s} c_i \vec{v}^{(i)^T} \left.\frac{\partial f^{ANN}}{\partial \vec{x}}\right\|_{\vec{x}^{(i)}} \left\{ -\frac{\rho_i}{P_i^{ref}} \cosh\left(f_i^{ANN}\right) \vec{b}^T \left.\frac{\partial f^{ANN}}{\partial \vec{x}}\right\|_{\vec{x}^{(i)}} g\left(\vec{H}^{(i)}\right)^T + \left(\vec{v}^{(i)^T} W^{(1)^T}\right) \circ g'^{\left(\vec{H}^{(i)}\right)^T} \right\}$
$\frac{\partial C_{pde}}{\partial W^{(1)}}$	$\frac{1}{N}\sum_i^{N_s} c_i \vec{v}^{(i)^T} \left.\frac{\partial f^{ANN}}{\partial \vec{x}}\right\|_{\vec{x}^{(i)}} \left\{ -\frac{\rho_i}{P_i^{ref}} \cosh\left(f_i^{ANN}\right) \vec{b}^T \left.\frac{\partial f^{ANN}}{\partial \vec{x}}\right\|_{\vec{x}^{(i)}} W^{(2)^T} \circ g'\left(\vec{H}^{(i)}\right)\vec{x}^{(i)^T} + W^{(2)^T} \circ g'\left(\vec{H}^{(i)}\right)\vec{v}^{(i)^T} + g''\left(\vec{H}^{(i)}\right) \circ W^{(2)^T} \circ \left(W^{(1)}\vec{v}^{(i)}\right)\vec{x}^{(i)^T} \right\}$
$\frac{\partial C_{pde}}{\partial \vec{\beta}}$	$\frac{1}{N}\sum_i^{N_s} c_i \vec{v}^{(i)^T} \left.\frac{\partial f^{ANN}}{\partial \vec{x}}\right\|_{\vec{x}^{(i)}} \left\{ -\frac{\rho_i}{P_i^{ref}} \cosh\left(f_i^{ANN}\right) \vec{b}^T \left.\frac{\partial f^{ANN}}{\partial \vec{x}}\right\|_{\vec{x}^{(i)}} W^{(2)^T} \circ g'\left(\vec{H}^{(i)}\right) + g''\left(\vec{H}^{(i)}\right) \circ W^{(2)^T} \circ \left(W^{(1)}\vec{v}^{(i)}\right) \right\}$
$\frac{\partial C_0}{\partial W^{(2)}}$	$\frac{1}{N_s}\sum_i^{N_s} c_i \left\{ \left(e_{2,i} + p_{2,i}\right) g\left(\vec{H}^{(i)}\right)^T + \left(\vec{r}^{(i)^T} W^{(1)^T}\right) \circ g'^{\left(\vec{H}^{(i)}\right)^T} \right\}$
$\frac{\partial C_0}{\partial W^{(1)}}$	$\frac{1}{N}\sum_i^{N_s} c_i \left\{ \left(e_{2,i} + p_{2,i}\right) W^{(2)^T} \circ g'\left(\vec{H}^{(i)}\right)\vec{x}^{(i)^T} + W^{(2)^T} \circ g'\left(\vec{H}^{(i)}\right)\vec{r}^{(i)^T} + g''\left(\vec{H}^{(i)}\right) \circ W^{(2)^T} \circ \left(W^{(1)}\vec{r}^{(i)}\right)\vec{x}^{(i)^T} \right\}$

$\frac{\partial C_0}{\partial \vec{\beta}}$	$\frac{1}{N}\sum_{i}^{N_s} c_i\{(e_{2,i} + p_{2,i})W^{(2)^T} \circ g'(\vec{H}^{(i)}) + g''(\vec{H}^{(i)}) \circ W^{(2)^T} \circ (W^{(1)}\vec{r}^{(i)})\}$

In the calculation of the gradients, table II, the symbol ∘ represents a Hadamard product which is given higher priority than standard matrix multiplication in the order of operations. Additionally, the quantity γ_i is a scalar quantity that takes a value of either 0 or 1. This value is determined by randomly sampling a uniform distribution on the range [0,1] and checking whether the drawn number is above or below a preset value. In this work the preset value was set to 0.9 meaning if the drawn number was less than 0.9 γ_i was set to 1 otherwise it was set to 0. The determination of γ_i was done for each training point on every epoch.

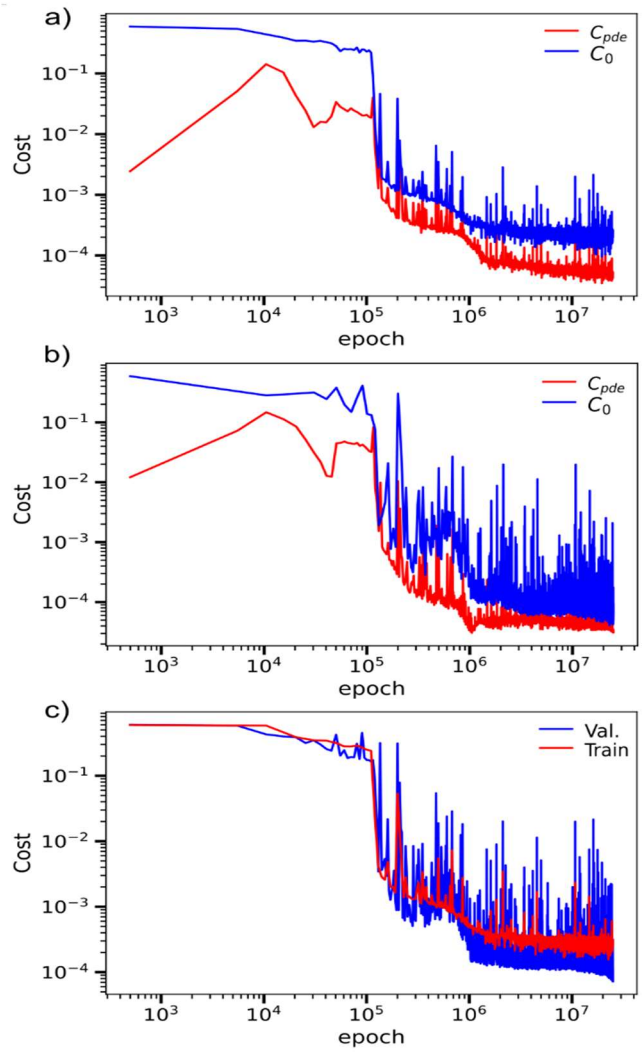

Figure S2: Learning curves for a) the training set and b) the validation set. The red curve is the cost associated with the portion of the cost based on the partial differential equation and the blue curve is the cost associated with the fractional error in the energies and pressures. C) provides a direct comparison of the total cost of the validation set, blue curve, with the total cost of the training set, red curve.

The resulting learning curves are shown in Fig. S2. Due to the stochastic nature built into the cost function there are many sharp peaks that form in both components of the cost as the instantaneous training set fluctuates. These sharp jumps tend to be significantly larger for C_0 which is due to training points at the matching boundary, 10^6 K where thermodynamic inconsistencies exist in the reference data, moving in and out of the instantaneous training set. Reducing the learning rate can reduce the magnitude of these spikes but results in a significantly longer training run. Removing the stochastic parameter γ and using all training data at each epoch would remove these spike but given C_{pde} works its way out of multiple local minimum at the onset of the training process, some level of stochasticity is beneficial in ensuring the model does not get stuck in these local minimum.

Shown in Fig. S3 is an analysis of the gradients of the ANN during the training process. Plotted are the max, average and minimum value of the distribution of the magnitude of the gradient associated with each weight matrix and bias vector. The gradients also show large spikes which can again be attributed to those training points at the matching boundary passing in and out of the instantaneous training set. The smallest gradients observed occur when the corresponding free parameter becomes relatively small compared to the rest of the free parameters. This analysis demonstrates that there are no issued with dead nodes arising during the training process for the case of an ANN with one single hidden layer consisting of 80 nodes.

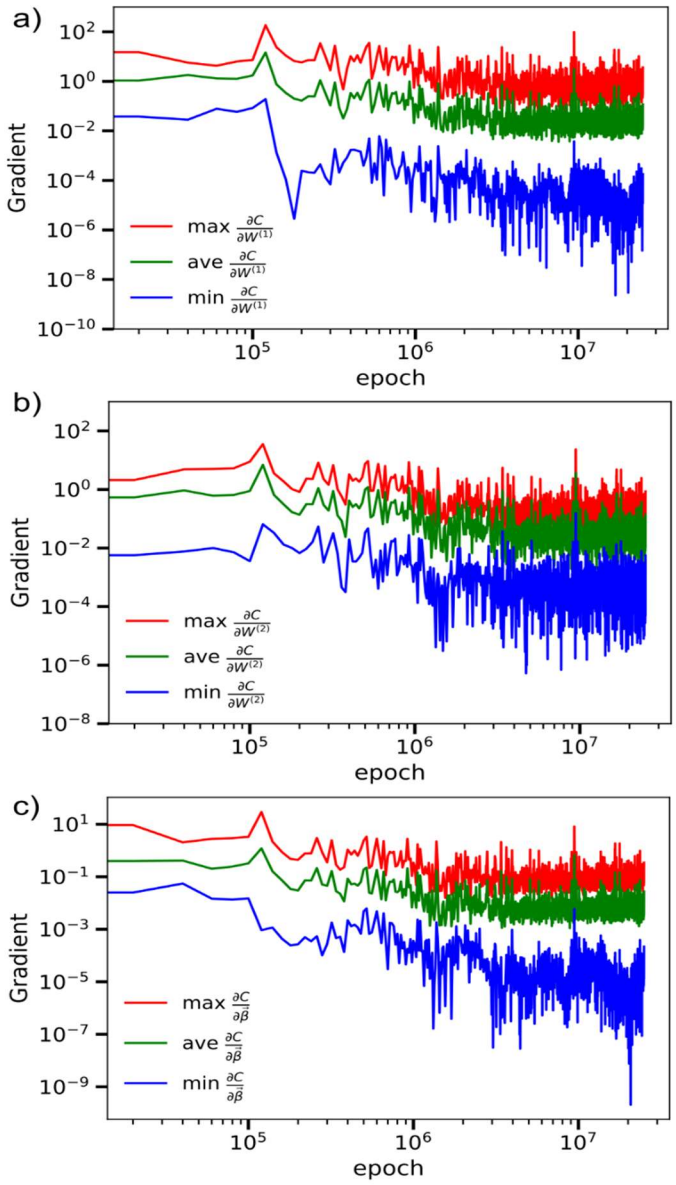

Figure S3: a), b) and c) provide the values of the gradients with respect to $W^{(1)}$, $W^{(2)}$, and $\vec{\beta}$ respectively. The red, green and blue curves provide the maximum, average and minimum, respectively, of the absolute value of the elements of the given matrix for the gradient of the total cost.

Section IV: Gradients of energy and pressure

In the analysis of the model the gradients of energy and pressure were utilized. These gradients were calculated analytically by taking the derivative of the energy and pressure with

respect to the input vector $\vec{x}$. After propagating the derivative through the neural network the resulting gradient of the energy is

$$\left.\frac{\partial E^{ANN}}{\partial \vec{x}}\right|_{\vec{x}^{(i)}} = \left(\cosh\left(f_i^{ANN}\right) - \sinh\left(f_i^{ANN}\right)\vec{a}^T \left.\frac{\partial f^{ANN}}{\partial \vec{x}}\right|_{\vec{x}^{(i)}}\right)\left.\frac{\partial f^{ANN}}{\partial \vec{x}}\right|_{\vec{x}^{(i)}} - \cosh\left(f_i^{ANN}\right) W^{(1)^T}\left(W^{(1)}\vec{a}\right) \circ W^{(2)^T} \circ g''\left(\vec{H}^{(i)}\right) \quad (3)$$

and the corresponding gradient of the pressure is

$$\left.\frac{\partial P^{ANN}}{\partial \vec{x}}\right|_{\vec{x}^{(i)}} = \rho_i^2 \cosh\left(f_i^{ANN}\right)\vec{b} + \rho_i \sinh\left(f_i^{ANN}\right)\left(\vec{b}^T \left.\frac{\partial f^{ANN}}{\partial \vec{x}}\right|_{\vec{x}^{(i)}}\right)\left.\frac{\partial f^{ANN}}{\partial \vec{x}}\right|_{\vec{x}^{(i)}} + \cosh\left(f_i^{ANN}\right) W^{(1)^T}\left(W^{(1)}\vec{b}\right) \circ W^{(2)^T} \circ g''\left(\vec{H}^{(i)}\right). \quad (4)$$

Here, the first and second elements of on the left-hand side of both Eq. (3) and (4) should be interpreted as the derivative with respect to the log of the temperature and the derivative with respect to the log of density respectively.

Section V: Stability tests

Table III: Test set performance on pressure as a function of the number of nodes in the hidden layer.

Dist.	Number of nodes in the hidden layer					
	20	40	60	80	100	120
min	0.223	0.058	0.066	0.015	0.063	0.069
25th	0.294	0.316	0.292	0.362	0.229	0.145
50th	0.517	1.025	0.530	0.587	0.685	0.298
75th	1.567	1.327	1.192	0.974	0.984	0.794
max	3.668	3.605	6.109	3.122	3.138	3.348

Table IV: Test set performance on energy as a function of the number of nodes in the hidden layer.

Dist.	Number of nodes in the hidden layer					
	20	40	60	80	100	120
min	0.003	0.225	0.002	0.002	0.009	0.011
25th	0.016	0.368	0.084	0.038	0.211	0.129
50th	0.412	0.5593	0.518	0.168	0.443	0.231

75th	1.118	1.276	1.524	0.992	1.488	0.882
max	25.441	26.632	26.898	25.475	24.311	25.454

To provide further insight into the model's performance additional test were conducted. For the first test the number of nodes in the hidden layer was varied from 20 to 120. For each case the PIML-EOS model was trained using the exact same training/validation/test sets described in the main text. The resulting errors on the pressure have been provided in Table III and the errors for energy are provided in Table IV. As can be seen the resulting error distributions are remarkably stable as a function of the number of nodes in the hidden layer. There are a few fluctuations in the overall shape of the error distributions, but each model is able to provide an accuracy for both energy and pressure on the order of 1 to 2%. The large errors made by each model are for the same points that can be found at the matching boundary. The resulting interpolations are consistent with one another with slight differences in their behavior at the low temperature boundary of the reference data set indicating extrapolation of the resulting EOS should be used with caution.

For the second stability test the training set size was varied. Using the initial training/validation/test split of 168/15/15, 42 points were moved from the training set to the test set to give a split of 126/15/57. Then starting with the 126/15/57 split an addition 42 points were moved from the training set to the test set to give a split of 84/15/99. For each of these 3 splits of the reference data a single model was trained where each model utilized 80 nodes in the hidden layer. Note that a given model is only trained and then applied to its specific data set split as to avoid biased results. The errors on the test set for both energy and pressure are provided in Table V and Fig. S4. As can be seen there appears to be a general shift of the error distribution for both pressure and energy to higher errors as the training set becomes smaller. However, on average the errors are still below 1%. Additionally, the points near the matching boundary are most sensitive to the training set size as can be seen in the max errors. Overall, this result supports the conclusion that the generalization error of the model with 168 should be on the order of 1%.

Table V: Test set performance as a function of the size of the training set.

Dist.	Pressure Training set size			Energy Training set size		
	168	126	84	168	126	84
min	0.015	0.014	0.003	0.002	0.004	0.007
25th	0.362	0.238	0.317	0.038	0.0233	0.227
50th	0.587	0.643	0.862	0.168	0.628	0.471
75th	0.974	0.989	1.509	0.992	1.208	1.197
max	3.122	5.628	5.213	25.475	26.759	25.542

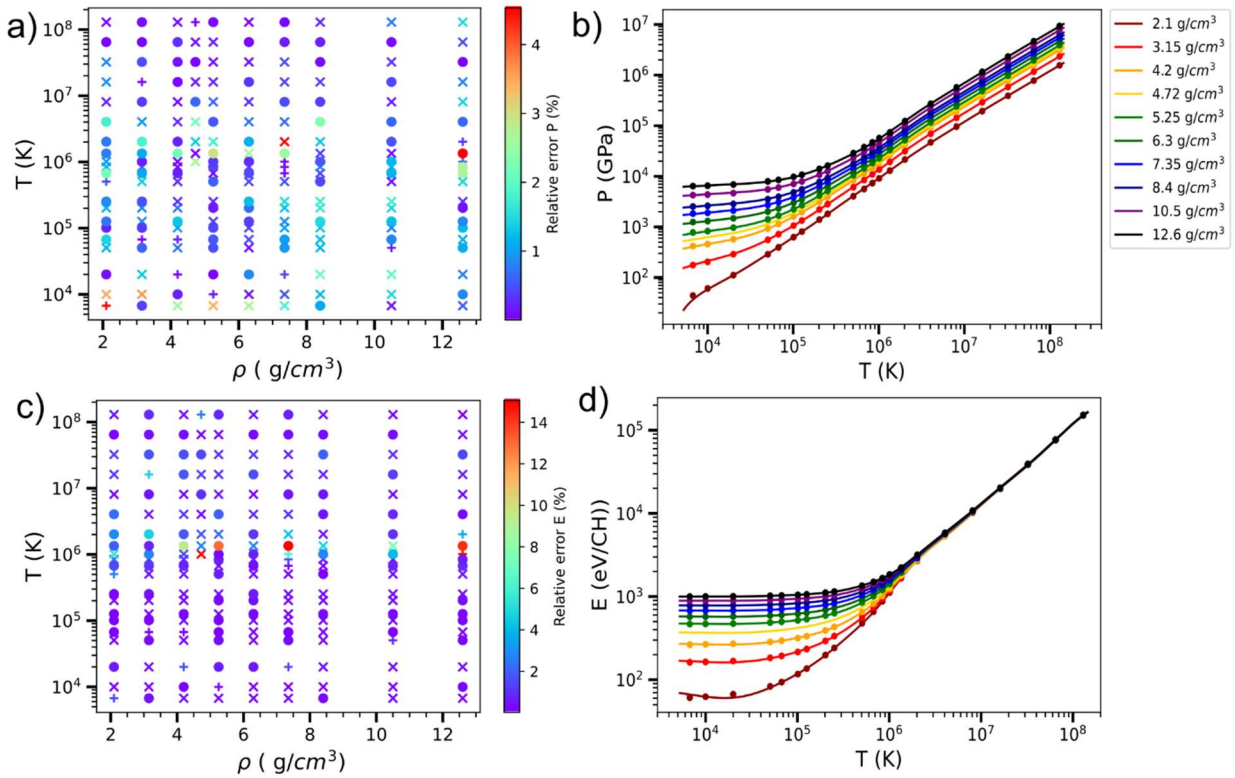

Figure S4: Errors and fits from the model trained with a training set size of 84. a) provides the errors in pressure across the domain of temperature and density considered. Circles are training points, + are validation points and x's are the test points. b) corresponding fits of the reference data which are indicated by circles. c) errors in the predicted energies. Symbols are the same as in a). d) corresponding fits of the energy.

Section VI: Cross-validation

To provide further validation a 5-fold cross validation is performed. For each fold a random sampling of the reference data set is performed to produce a training/validation/test split of 168/15/15. An ANN with a single hidden layer consisting of 80 nodes is then trained on each fold. The resulting errors on the test set can be found in Table VI. Across all 5 members of the ensemble the errors are consistently below 1% for both pressure and energy. The most noticeable difference is in the high error tail on the error distributions associated with the predicted energies. The points comprising this tail are those found near the matching boundary. This suggests the sampling of points around a potential thermodynamic inconsistency is important for minimizing the model's errors at the inconsistency.

Table VI: Test set performance for the members of the 5-fold cross validation.

	Pressure					Energy				
	Ensemble member					Ensemble member				
Dist.	1	2	3	4	5	1	2	3	4	5
min	0.015	0.170	0.234	0.010	0.013	0.002	0.043	0.091	0.020	0.025
25th	0.362	0.372	0.354	0.087	0.198	0.038	0.088	0.165	0.100	0.146

50th	0.587	0.531	0.772	0.167	0.469	0.168	0.111	0.254	0.315	0.428
75th	0.974	1.514	1.169	0.891	0.773	0.992	1.163	1.126	0.647	0.704
max	3.122	3.056	3.243	3.131	3.038	25.475	37.368	38.222	24.368	40.630

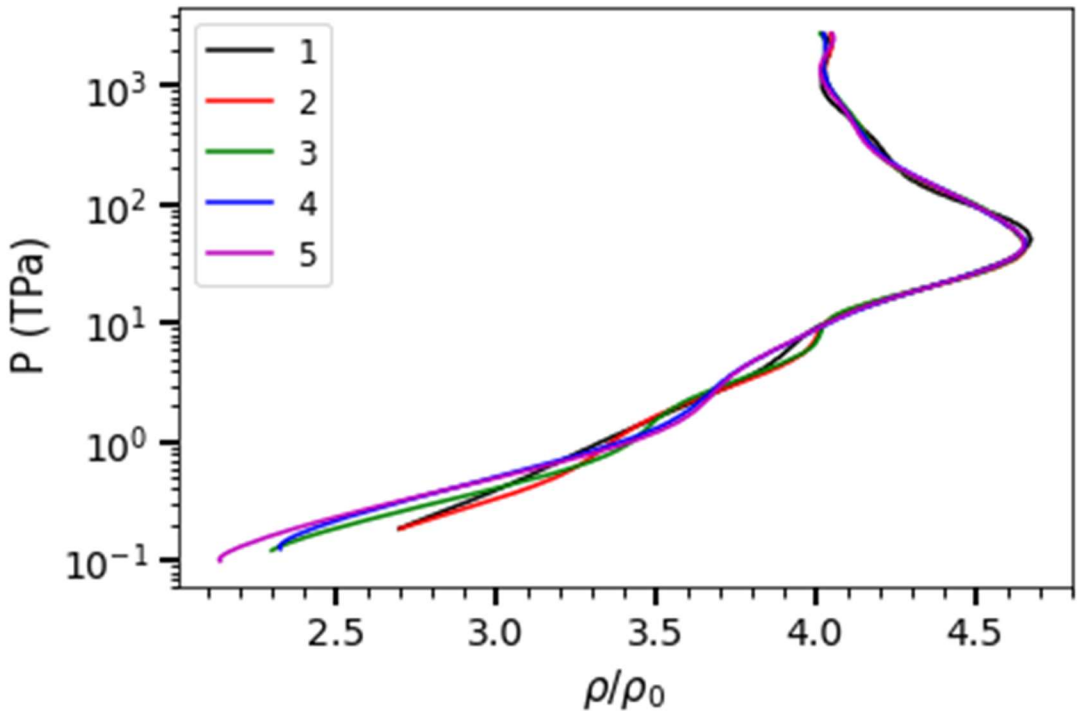

Figure S5: Hugoniot from each of the models from the 5-fold cross validation.

Provided in Fig. S5 are the predicted Hugoniot from each of the members of the 5-fold cross validation. While the error distributions for energy and pressure are comparable across all 5 of the members of the ensemble, the resulting Hugoniots appear to be highly sensitive on the minor differences. This spread in the predicted Hugoniot can be seen as an uncertainty on the model's predictions. When applicable such an ensemble approach can be used to estimate the uncertainties in energy and pressure enabling the user to determine thermodynamic conditions where additional reference data may be needed.